Open Archive TOULOUSE Archive Ouverte (OATAO)

OATAO is an open access repository that collects the work of Toulouse researchers and makes it freely available over the web where possible.

Any correspondence concerning this service should be sent to the repository administrator: staff-oatao@listes-diff.inp-toulouse.fr

Dog-bone copper specimens prepared by one-step spark plasma sintering

Claire Arnaud[1,2] · Charles Manière[1,3] · Geoffroy Chevallier[1,4] · Claude Estournès[1,4] ·
Ronan Mainguy[5] · Florence Lecouturier[2] · David Mesguich[1] · Alicia Weibel[1] ·
Lise Durand[3] · Christophe Laurent[1]

Abstract Copper dog-bone specimens are prepared by one-step spark plasma sintering (SPS). For the same SPS cycle, the influence of the nature of the die (graphite or WC–Co) on the microstructure, microhardness, and tensile strength is investigated. All samples exhibit a high Vickers microhardness and high ultimate tensile strength. A numerical electro-thermal model is developed, based on experimental data inputs such as simultaneous temperature and electrical measurements at several key locations in the SPS stack, to evaluate the temperature and current distributions for both dies. Microstructural characterizations show that samples prepared using the WC–Co die exhibit a larger grain size, pointing out that it reached a higher temperature during the SPS cycle. This is confirmed by numerical simulations demonstrating that with the WC–Co die, the experimental sample temperature at the beginning of the dwell is higher than the experimental control temperature measured at the outer surface of the die. This difference is mostly ascribed to a high vertical thermal contact resistance and a higher current density flowing through the WC–Co punch/die interface. Indeed, simulations show that current density is maximal just outside the copper sample when using the WC–Co die, whereas by contrast, with the graphite die, current density tends to flow through the copper sample. These results are guidelines for the direct, one-step, preparation of complex-shaped samples by SPS which avoids waste and minimizes machining.

✉ Christophe Laurent
laurent@chimie.ups-tlse.fr

Claire Arnaud
arnaud@chimie.ups-tlse.fr

Charles Manière
maniere@chimie.ups-tlse.fr

Geoffroy Chevallier
chevallier@chimie.ups-tlse.fr

Claude Estournès
estourne@chimie.ups-tlse.fr

Ronan Mainguy
Ronan.Mainguy@ensiacet.fr

Florence Lecouturier
florence.lecouturier@lncmi.cnrs.fr

David Mesguich
mesguich@chimie.ups-tlse.fr

Alicia Weibel
weibel@chimie.ups-tlse.fr

Lise Durand
lise.durand@cemes.fr

[1] Université de Toulouse, Institut Carnot CIRIMAT, UMR CNRS-UPS-INP 5085, Université Paul-Sabatier, 118 route de Narbonne, 31062 Toulouse Cedex 9, France

[2] Laboratoire National des Champs Magnétiques Intenses, UPR CNRS-UPS-INSA-UJF 3228, 143 avenue de Rangueil, 31400 Toulouse, France

[3] CEMES, UPR CNRS 8011, Université de Toulouse, 29 rue Jeanne Marvig, 31055 Toulouse, France

[4] Plateforme Nationale CNRS de Frittage Flash, PNF2, MHT, Université Paul-Sabatier, 118 route de Narbonne, 31062 Toulouse Cedex 9, France

[5] Université de Toulouse, Institut Carnot CIRIMAT, UMR CNRS-UPS-INP 5085, INPT/ENSIACET, 4 allée Emile Monso, BP44362, 31030 Toulouse Cedex 4, France

Introduction

Spark plasma sintering (SPS) and other electric field-assisted sintering techniques become more widespread for the rapid fabrication of all kinds of materials and composites because of several advantages over pressureless sintering and hot-pressing, including lower sintering temperatures and shorter holding times [1, 2]. Near-net-shape manufacturing technologies produce parts that are close to the finished size and shape, requiring a minimal amount of finishing process such as machining and also avoiding waste. The potential of SPS for near-net-shaping has been recognized and some studies have reported the formation of complex-shaped samples, with more or less pronounced deviations from the cylindrical symmetry, for materials as diverse as porous silica monoliths [3], oxide composites [4], silicon carbide [5], coatings on Ni-based superalloys [6], and TiAl alloys [7]. However, so far there are only a few studies addressing the problem theoretically [8–10], investigating the impact of the sample geometry, size and heterogeneous stress states on the non-uniformity of temperature, relative density, and grain size spatial distributions. The aim of this paper is to investigate the direct preparation by SPS of copper samples with the so-called dog-bone shape used for tensile tests specimens. For the same SPS cycle, the influence of the nature of the tailor-made die (graphite or WC–Co) on the microstructure, microhardness, and ultimate tensile strength (UTS) of the copper specimen is investigated. Electro-thermal modeling was performed in order to investigate any difference that might occur because of the different nature of the dies.

Experimental

Sample preparation

A commercial copper powder (Alfa Aesar, 99 %, polyhedral grains, 1.0 ± 0.5 μm) was used. Dog-bone specimens were prepared in one step by SPS (Dr. Sinter 2080, SPS Syntex Inc., Japan). The tailor-made die was either made up of graphite (Mersen, Graphite G2333) or WC–Co (Pedersen, WC–Co 93.5: 6.5 wt%). Other than that, everything else was similar. The inner wall of the die was coated with a graphite layer deposited by spray. A sheet of graphitic paper (Mersen, Papyex® N998, 0.2-mm thick) was placed between the top and bottom graphite punches and the powder for easy removal. The SPS run was performed in vacuum (residual cell pressure <10 Pa). The default pattern of the machine, twelve current pulses followed by two periods of zero currents, was used. The temperature was controlled using a thermocouple (DME31, type K) introduced in a hole (3-mm deep) located on the outer surface of the die. The sample (green density 56 %, initial thickness 3.4 mm) was heated from room temperature to 700 °C (50 °C min^{-1}), where a 6 min dwell was applied. The minimal uniaxial charge (corresponding to 1 MPa on the compact) was applied during the ramp. Then, a uniaxial charge (corresponding to 8 MPa on the compact) was gradually applied within the first minute of the dwell at 700 °C and maintained during the remaining 5 min. Cooling was applied down to room temperature (100 °C min^{-1}) and the uniaxial load was gradually released during the same time. The graphitic paper remaining on the surface was removed by polishing. The dog-bone samples were 53-mm long with a gage 16-mm long, 3-mm wide, and 1.7-mm thick. The specimens

Fig. 1 Schematic representation of the stack: materials involved (**a**) and the contact interfaces that contribute to the electric and thermal contacts resistances (CR) (**b**)
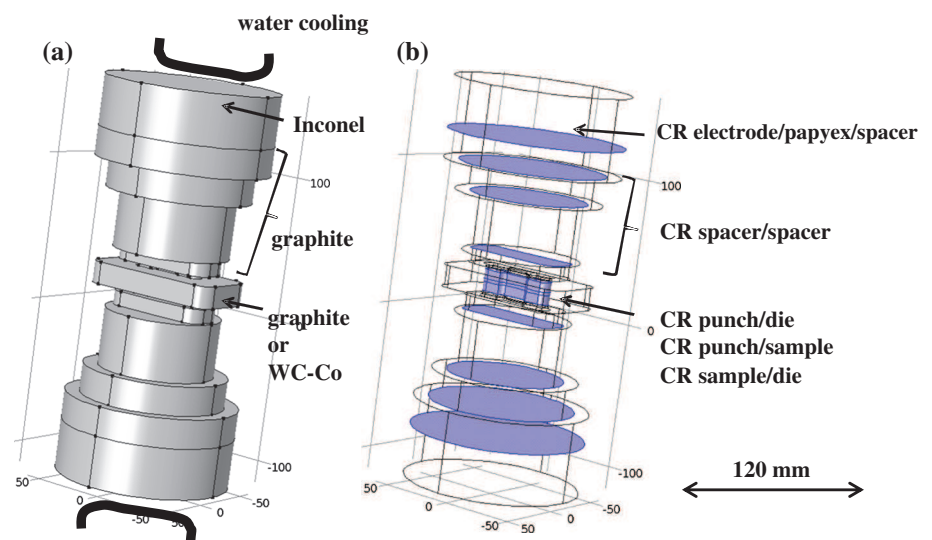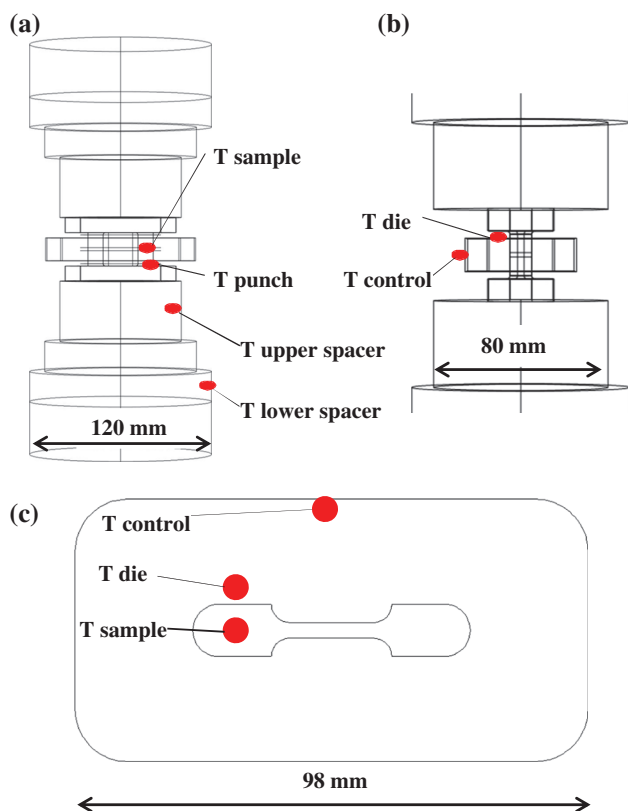
Fig. 2 Position of the six thermocouples: lower and upper spacers, punch, sample (**a**); control, die (**b**) and horizontal cross-section of the die, showing position details (**c**)

are hereafter denoted SG and SWC, respectively, where G stands for graphite and WC for WC–Co. The dies are denoted DG and DWC.

Following earlier works performed on this particular SPS machine [11], a specific instrumentation was developed to perform simultaneous temperature measurements at several locations in the SPS stack and electrical measurements across it, giving real time thermal and electrical conditions of the stack during the sintering cycle. The contact interfaces between its constitutive elements (punches, spacers, die, and sample) show a variety of pressure and temperature conditions and contribute to electric and thermal contact resistances (ECR and TCR, respectively) (Fig. 1). Earlier studies [12–17] showed that horizontal contact resistances are lower than vertical ones, the latter being reportedly the main cause of the temperature difference between the sample core and the surface of the outer die. The ECR and TCR were calibrated using experimental temperatures and for this purpose six thermocouples were placed in the appropriate places in the stack (Fig. 2). In particular, the sample thermocouple is embedded within the powder in one of the dog-bone heads (Fig. 2c). All calibrated ECR and TCR are reported in the Appendix (Table 1). The root-mean-square (RMS) current used as an input for the current density is measured

experimentally by a Rogowski coil sensor placed on the current exit under the SPS chamber. Then, the different values collected were used as input data to a numerical electro-thermal model. The local conditions were modeled in order to investigate any difference that might occur because of the different nature of the dies, the thermal and pressure cycles being exactly the same at the macroscopic scale. The equations used for the Joule heating model (heat equation, current equation), the thermal model, and the electric and thermal contacts at the inner interfaces, as well as the relevant physical properties of Inconel, graphite, WC–Co, and copper are given in the Appendix (Table 2).

Characterization

The density of the dog-bone specimens was measured by Archimedes' method and their relative density was calculated using 8.96 g cm^{-3} as the theoretical density of copper. Microhardness was determined from indentation tests (1 N for 10 s in air at room temperature) performed on the polished surface along the length, from one head to the other, of the dog-bone specimen. Loading was applied with a Vickers indenter (Shimadzu HMV M3). The spacing between neighboring indents was 10 times the diagonal length of the indent. Tensile tests (MTS Synergie 1000) were performed at room temperature. Two SG and two SWC samples were tested. Precise stresses were measured by a 5 kN stress gauge system (crosshead displacement 6×10^{-5} m s^{-1} and equivalent strain rate is 3.75×10^{-3} s^{-1}). The elongation was measured with an extensometer. Fracture surfaces were observed by scanning electron microscopy (SEM, JEOL JSM 6700F).

Results and discussion

The relative density of the copper dog-bone specimens is similar for SG (98 ± 1 %) and SWC (97 ± 1 %). Starting from one end of the dog-bone sample, the Vickers microhardness (Fig. 3) slightly but gradually decreases, reaching a minimum for the shoulder, then increases to a value close to the initial one for the middle of the gage length. Then, it follows a roughly symmetrical evolution, as could be expected from the geometry of the SPS stack. This evolution along the length of the specimen, less pronounced for SG than for SWC, could reflect a variation in copper grain size due to differences in the actual temperature reached in different parts of the sample, the parts with a lower grain size showing a higher microhardness. The average microhardness values, higher for SG (about 1.26 GPa) than for SWC (about 1.11 GPa), are in line with values reported by other authors [18, 19] for SPS copper samples with a grain size in the range 0.4–0.7 µm.
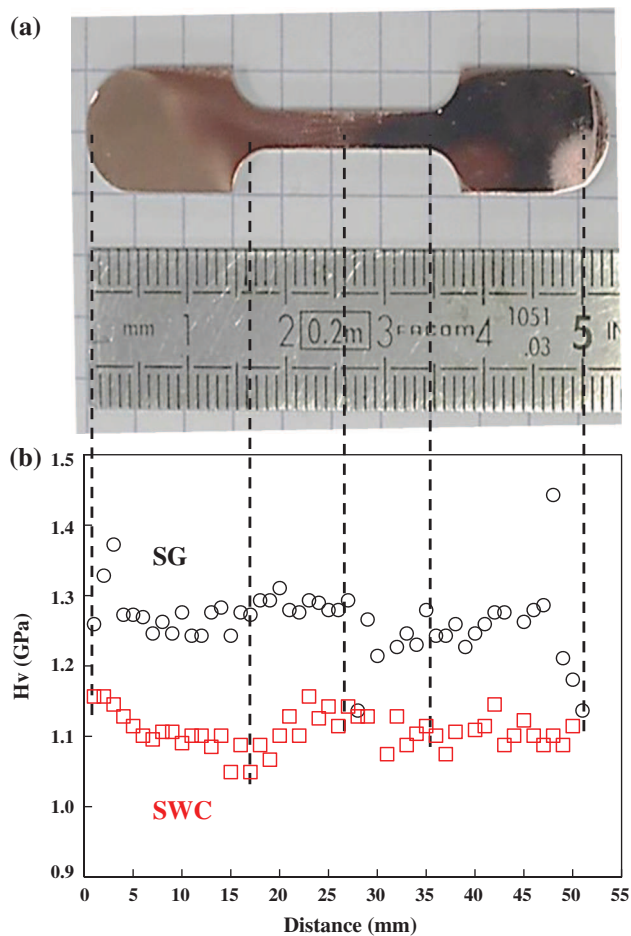
(a)

(b)

Fig. 3 Photograph of a dog-bone specimen (**a**) and Vickers microhardness versus the distance from one end of the dog-bone (**b**). The *dotted lines* are guides to the eye

Fig. 4 Tensile stress–strain curves of SG and SWC

(a)

(b)

Fig. 5 SEM images of the fracture surfaces of SG (**a**) and SWC (**b**). Different detectors of secondary electrons were used: detector in the objective lens (**a**) and in the microscope chamber (**b**). *Arrows* in **b** point out two dimples with very different sizes

The stress–strain curves are reported in Fig. 4. The Young modulus is about 100 GPa for all samples, lower than the value (115 GPa) found for conventional cast copper [20], which could reflect heterogeneities in grain size and porosity, in line with the microhardness fluctuations. The UTS is higher for the SG samples (382 and 348 MPa, average 365 MPa) than for the SWC samples (322 and 284 MPa, average 303 MPa). The drop in the stress–strain curve at the end of the elastic region is characteristic of the yield point phenomenon [21]. Variations in tensile response are observed, probably induced by microstructure heterogeneities along the gage length as also evidenced on the microhardness profile. A higher elongation could reflect a larger grain size. SEM images of the fracture surfaces of the tensile test specimens reveal the typical dimples mostly below 1 µm in size for SG (Fig. 5a), indicating negligible grain growth during sintering and a bimodal microstructure for SWC, most grains about 1 µm in size with some areas (about 25–30 % of the
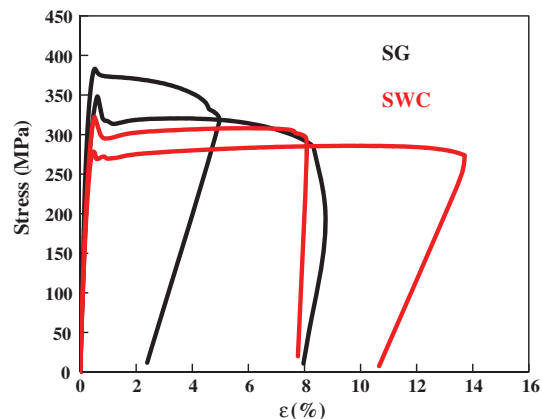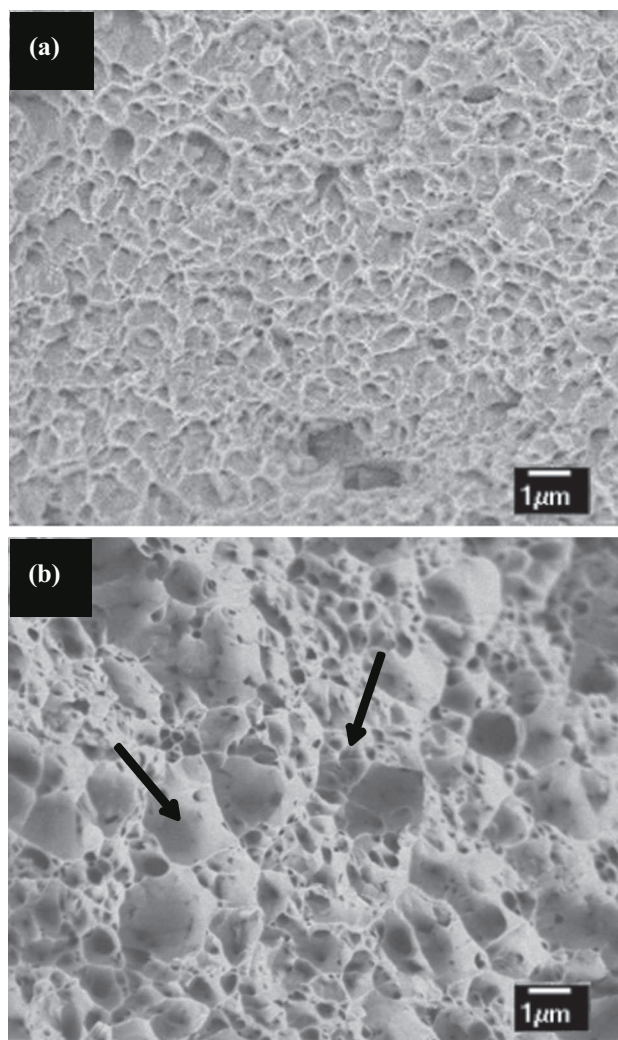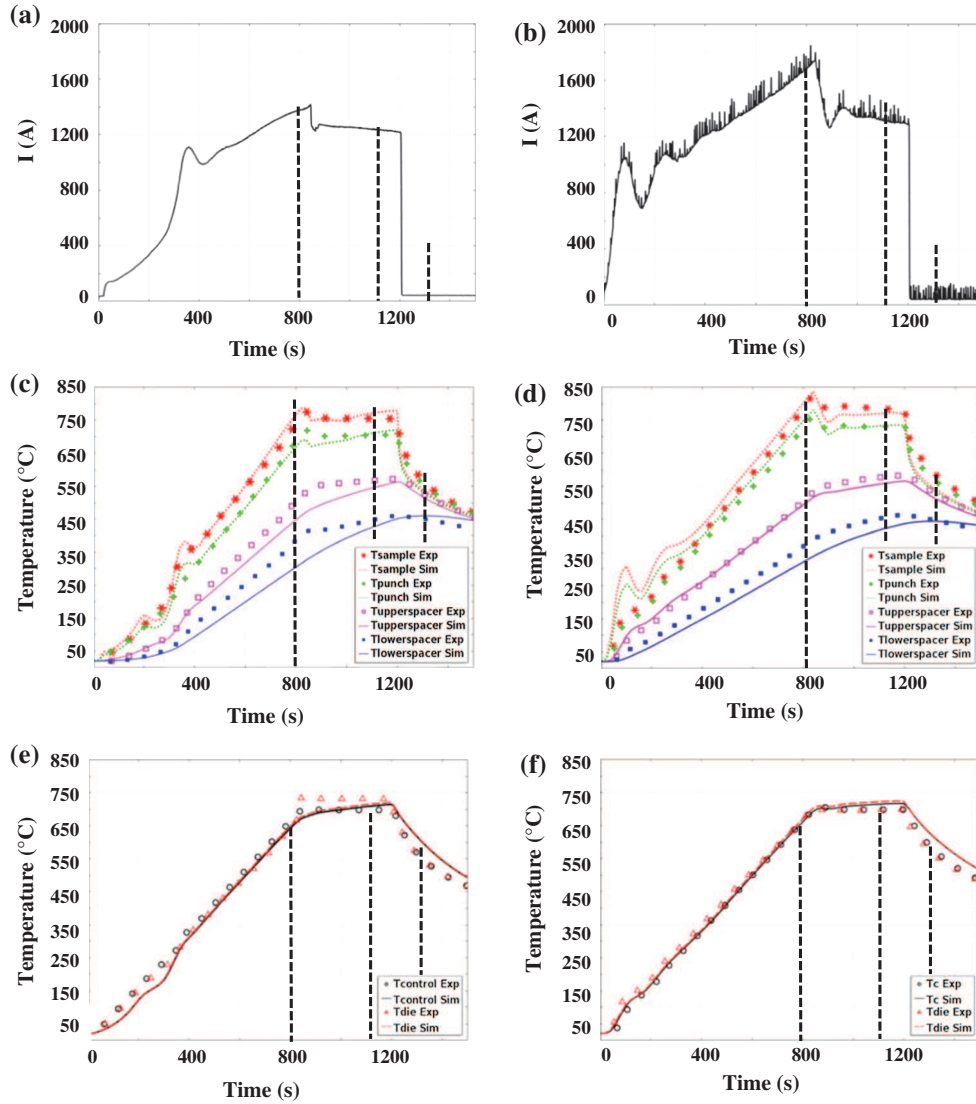
Fig. 6 RMS current profiles for the graphite die (**a**) and the WC–Co die (**b**). Simulated and experimental temperature profiles for the graphite die (**c**, **e**) and the WC–Co die (**d**, **f**). The *vertical dotted lines* indicate times (800, 1100, and 1300 s) discussed in the text

total observed area) showing signs of a clear but limited grain growth up to about 2 μm (Fig. 5b). Note that the apparent difference in contrast is due to different secondary electrons detectors being used: in-objective lens detector (Fig. 5a) and detector in microscope chamber (Fig. 5b). These results are in agreement with other reports [22] showing that, starting from a micrometric powder, the average copper grain size of a specimen prepared by SPS at 800 °C is about three times larger than when it is prepared at 750 °C (6.6 and 2.2 μm, respectively). Pores about 100–200 nm in size are observed for both specimens, which could account for the residual porosity (2–3 %).

The above results show that the grain size for SWC is larger than that for SG at least in some areas including the tensile test area. This could suggest that the SWC sample reached a higher temperature during the SPS cycle.

Considering that the thermal and pressure cycles were exactly the same at the macroscopic scale, this difference can only be ascribed to the different nature of the dies.

The RMS current profile versus time is presented for the SPS runs with DG (Fig. 6a) and DWC (Fig. 6b). The maximum current intensity is 1413 A for DG and 1746 A for DWC, reflecting that DWC requires a higher heating power because the electrical conductivity of WC–Co is higher than that of graphite. Oscillations of the RMS current are observed throughout the thermal cycle, notably for DWC. As discussed later in the paper, this reflects the lag of thermal response of the die to the current signal. The CR calibration method is performed using an inverse analysis approach, which is very efficient to determine a set of ECR and TCR values without requiring a lengthy experimental campaign. Firstly, a model without contact is implemented.

Fig. 7 Simulation of the temperature distribution for the vertical cross-section of the stack, in the heating regime (800 s), during the dwell (1100 s) and during cooling down (1300 s) for the graphite die (*upper panel*) and the WC–Co die (*lower panel*)
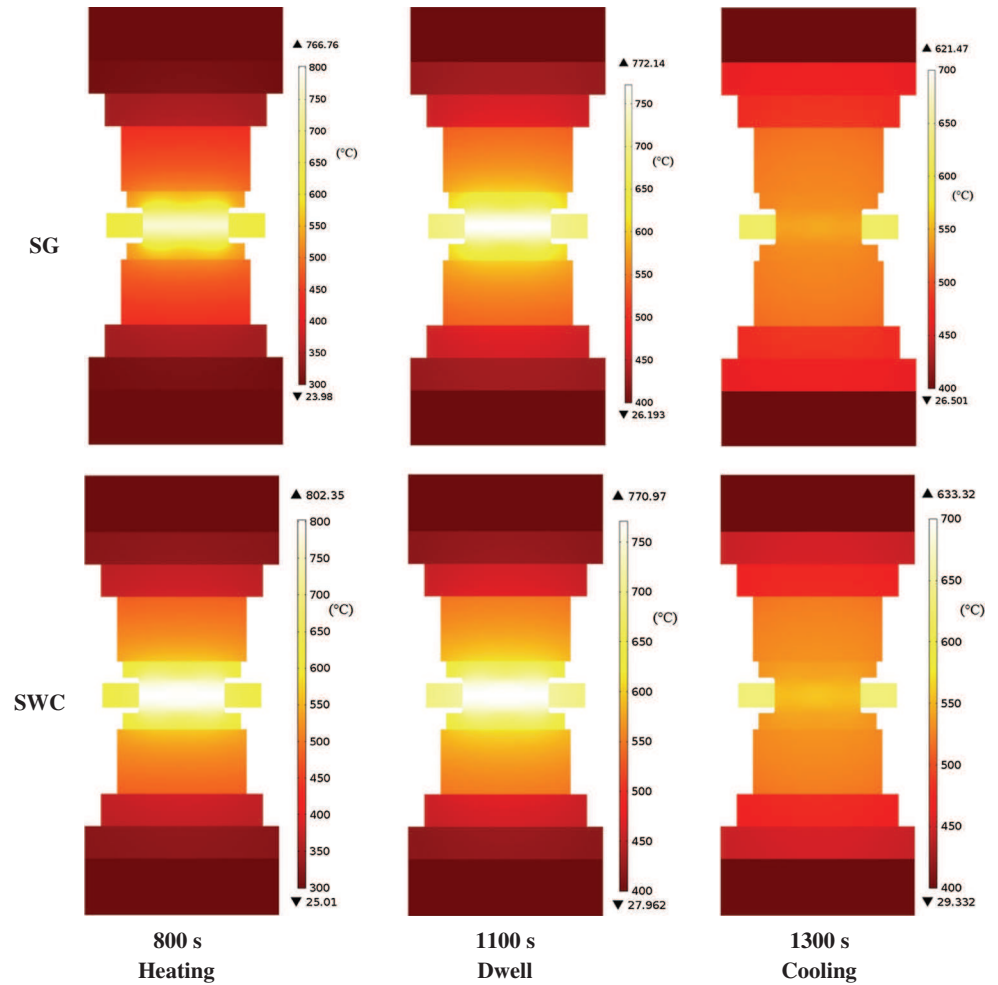
The heat dissipated in the column is underestimated because this first model does not take the ECR into account. Indeed, temperatures simulated with the first model are lower than the measured temperatures. Then, in order to raise the overall temperature field, ECR are first introduced, starting from the contact interfaces of the electrodes to the center of the column (punches, die, and sample). All the simulated temperatures are adjusted to the experimental temperatures in the best possible way. At this stage, the overall simulated/experimental temperature differences are roughly equal to 100 K. This is due to the absence of the TCR responsible for high thermal gaps at all interfaces in the column, especially for the sample, punches, and die. In a third step, the TCR are then introduced in the simulation starting from the electrode to the center of the column. The simulated temperature field is adjusted to fit the temperature differences observed experimentally. The ECR from the second calibration step are also adjusted to find the best agreement with the experimental temperatures. Finally, the cooling regime is studied to verify the

TCR calibrated values. Indeed, this regime is a pure thermal problem because there is no current passing through the column. If wrong TCR values are calibrated and compensated by wrong ECR values, the cooling regime can be used to identify this problem and help to correct it. The simulated and experimental temperature profiles after calibration of all the ECR and TCR (Appendix—Table 1) are reported in Fig. 6c, d, e, f.

At the beginning of the dwell (844 s), the experimental sample temperature is higher than the experimental control temperature, by a value of 76 °C for DG (Fig. 6c) and 125 °C for DWC (Fig. 6d). Thus, it is interesting to note that the SWC sample reached 825 °C, i.e., about 50 °C higher than SG. During the dwell (1100 s), there is still a 30 °C difference, in both cases, between experimental control temperature and experimental sample temperature. Moreover, the experimental punch temperature (not shown) is higher than the experimental control temperature (23 and 62 °C at 800 s for DG and DWC, respectively). This shows that the heating of the die lags behind the heating of the

Fig. 8 Simulation of the temperature distribution for the horizontal cross-section of the stack, in the heating regime (800 s), during the dwell (1100 s) and during cooling down (1300 s) for the graphite die (*upper panel*) and the WC–Co die (*lower panel*)
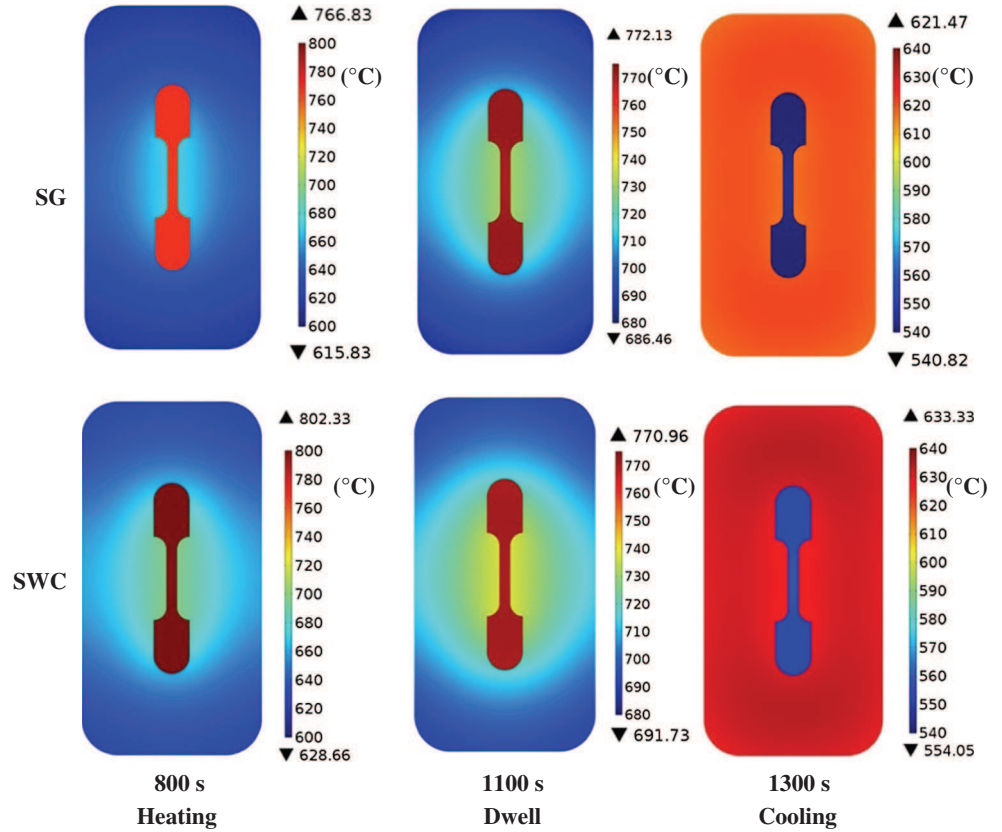
punch, which could reflect a vertical TCR. The temperatures in the heating regime (800 s), during the dwell (1100 s) and during cooling down (1300 s) were simulated for the vertical cross-section of the stack (Fig. 7). The effects of the TCR are observed at each interface, a temperature gap creating a color gap in the simulation images. In the heating, dwell, and cooling regimes, the maximum temperature (i.e., the temperature of the sample) is higher for SWC than for SG. These results are also observed for the horizontal vertical cross-section (Fig. 8). This could confirm the presence of the high vertical punch/die TCR, which is equal to about 0.002 K m^2 W^{-1} and creates a thermal gap between punch and die roughly equal to 90 °C in the heating regime. As shown by other authors [23], the vertical punch/die TCR is very high because of the low contact pressure applied there. The simulation and experimental results both show that the sample reaches a higher temperature with DWC than with DG, which could account the larger grain size for SWC, and thus confirms what was suspected from the microhardness and tensile tests.

The punch/die ECR and TCR for both DG and DWC converge to values near 2 × 10^{-7} Ω m^2 and 0.002 K m^2 W^{-1} at 800 s. Simulations show that current density at 800 s (Fig. 9) significantly increases through SG. By contrast, it is maximal in DWC just outside the SWC sample. The heat dissipated at the

punch/die interface is higher for DWC. Moreover, for DWC, both the punch/spacer ECR and TCR are higher at high temperatures (1.67 × 10^{-8} Ω m^2 and 2 × 10^{-4} K m^2 W^{-1}, respectively) and contribute to dissipate and maintain more heat inside the punches/sample area. These are the main causes of the 50 °C sample temperature difference observed between the two samples. The difference in current density flowing through the copper sample, as revealed in Fig. 9, probably has some influence on its final density and microstructure, which warrants further studies. Other authors [24] have shown that the copper sintering rate is significantly increased in current-assisted sintering compared to a current-insulated configuration. Moreover, the high punch/die TCR for DWC could account for the regulation difficulties observed in the RMS current profile (Fig. 6b).

Conclusions

It is shown that it is possible to prepare copper dog-bone specimens by one-step SPS. For the same sintering cycle, there is a significant influence of the nature of the dog-bone-shaped die (graphite or WC–Co) on the microstructure, microhardness, and tensile strength of the copper
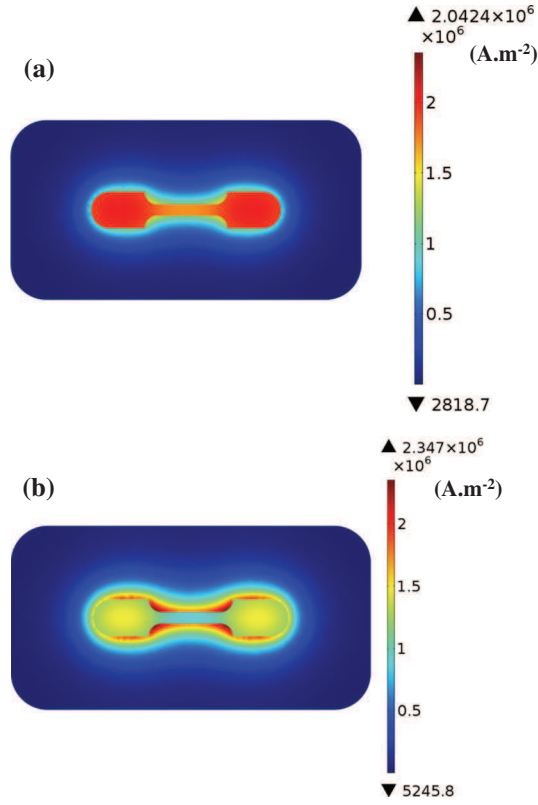
Fig. 9 Simulation of the current density distribution for the horizontal cross-section of the stack, in the heating regime (800 s), for the graphite die (**a**) and the WC–Co die (**b**)

samples. The SG and SWC samples exhibit a high Vickers microhardness (130 and 110 GPa, respectively) and high UTS (365 and 303 MPa, respectively). The lower mechanical properties for SWC compared to SG result from the larger grain size of SWC samples, as is confirmed by microstructural characterizations. In turn, one can reasonably assume that this larger grain size is due to higher sintering temperature, although the same SPS parameters have been used for all samples (apart from the nature of the die). This was effectively confirmed by using a specific instrumentation allowing one to perform simultaneous temperature measurements at several locations in the SPS stack and electrical measurements across it, used as input data to a numerical electro-thermal model. Due mostly to vertical thermal contact resistance at the punch/die interface (about 0.002 K m^2 W^{-1}) and a higher current density flowing through the WC–Co punch/die interface, the experimental SG and SWC sample temperature at the beginning of the dwell (775 and 825 °C, respectively) are higher than the experimental control temperature measured at the outer surface of the die (700 °C). With the WC–Co die, the sample reaches a higher temperature (50 °C) than

with the graphite die, resulting in the larger grain size of the copper sample. Simulations show that with the graphite die, the current density tends to flow through the copper sample, whereas by contrast, the current density is maximal just outside the copper sample when using the WC–Co die. This probably has some influence on its final density and microstructure, which warrants further studies. These results are important guidelines for future works on the direct, one-step, preparation of complex-shaped samples by SPS, which avoids waste and minimizes machining. The basic advantages of SPS (lower sintering temperatures and shorter holding times), which allow one to manufacture samples with finer or altogether different microstructures, still hold true for near-net-shaping and it is the opinion of the present authors that its merit in comparison to alternate routes (including machining, rolling, forging, extrusion, etc.) will emerge and be recognized in the not too distant future. Future works include optimizing the SPS cycle in order to increase the homogeneity of density and most importantly grain size within the sample.

Appendix

The Joule heating model obeys to the heat Eq. (1) and the current Eq. (2):

$$\nabla(-\lambda\nabla T) + \rho C_p \frac{\partial T}{\partial t} = \mathrm{JE} \tag{1}$$

$$\nabla\vec{J} = \nabla(\sigma\vec{E}) = 0 \tag{2}$$

with E the electric field, J the current density, λ the thermal conductivity, σ the electric conductivity, Cp the heat capacity, ρ the density, and T the temperature. The relevant physical properties are given in Tables 1 and 2.

The thermal model uses two main boundary conditions. Surface radiation is governed by Eq. (3):

$$\phi_r = \sigma_s \cdot \varepsilon \cdot \left(T_e^4 - T_a^4\right) \tag{3}$$

with ϕ_r the radiative heat flux, σ_s the Stefan–Boltzmann's constant (5.6704 × 10^{-8} W m^{-2} K^{-4}), ε the emissivity (0.80 for graphite and 0.85 for WC–Co), T_a the chamber wall temperature, and T_e the emission surface temperature. The heat flux at the level of the water cooling system obeys Eq. (4):

Table 1 All calibrated electric and thermal contact resistances (ECR and TCR, respectively) for SPS runs using the graphite die (DG) and the WC–Co die (DWC)

Contact	Type of contact	DG	DWC
Electrode/spacer	ECR ($\Omega\ m^2$)	2×10^{-7}	2×10^{-8}
	TCR ($K\ m^2\ W^{-1}$)	1	0.17
Spacer/spacer	ECR ($\Omega\ m^2$)	2×10^{-7}	2×10^{-8}
	TCR ($K\ m^2\ W^{-1}$)	1×10^{-3}	1.25×10^{-3}
Spacer/punch	ECR ($\Omega\ m^2$)	$3 \times 10^{-9}\left(\frac{3000-T}{T-100}\right)^{1.3}$	1.67×10^{-8}
	TCR ($K\ m^2\ W^{-1}$)	$6 \times 10^{-5} + 4 \times 10^{-5}\left(\frac{1000-T}{T-50}\right)^2$	2×10^{-4}
Punch/sample	ECR ($\Omega\ m^2$)	$4 \times 10^{-8}\left(\frac{2200-T}{T-100}\right)^{1.6}$	$4 \times 10^{-8}\left(\frac{2800-T}{T-100}\right)^{1.2}$
	TCR ($K\ m^2\ W^{-1}$)	$3 \times 10^{-5} + 4 \times 10^{-5}\left(\frac{1000-T}{T-50}\right)^2$	$3 \times 10^{-5} + 4 \times 10^{-5}\left(\frac{1000-T}{T-100}\right)^2$
Vertical contact	ECR ($\Omega\ m^2$)	$8 \times 10^{-8}\left(\frac{3000-T}{T-50}\right)^{1.2}$	$6 \times 10^{-8}\left(\frac{2700-T}{T-50}\right)$
	TCR ($K\ m^2\ W^{-1}$)	$2 \times 10^{-3} + 1.5 \times 10^{-4}\left(\frac{2500-T}{T-50}\right)^{2.2}$	$1 \times 10^{-3} + 1.5 \times 10^{-4}\left(\frac{2500-T}{T-50}\right)^2$

Table 2 Physical properties of Inconel, graphite, WC–Co, and copper (with T in Kelvin)

Material	Heat capacity C_p ($J\ kg^{-1}\ K^{-1}$)	Thermal conductivity λ ($W\ m^{-1}\ K^{-1}$)	Electrical resistivity ρ_e ($\Omega\ m$)	Density ρ ($kg\ m^{-3}$)
Inconel	$344 + 2.50 \times 10^{-1}\ T$	$10.1 + 1.57 \times 10^{-2}\ T$	$9.82 \times 10^{-7} + 1.6 \times 10^{-10}\ T$	8430
Graphite	$34.27 + 2.72\ T - 9.60 \times 10^{-4}\ T^2$	$123 - 6.99 \times 10^{-2}\ T + 1.55\ \times 10^{-5}\ T^2$	$1.70 \times 10^{-5} - 1.87 \times 10^{-8}\ T + 1.26 \times 10^{-11}\ T^2 - 2.44 \times 10^{-15}\ T^3$	$1904 - 0.01414\ T$
WC–Co	$4.76 \times 10^6\ T^{-2} + 2.22 \times 10^2 + 4.40 \times 10^{-2}\ T - 5.13 \times 10^{-6}\ T^2$	$94.4 - 3.82 \times 10^{-2}\ T + 7.98 \times 10^{-6}\ T^2$	$4.34 \times 10^{-13}\ T^2 + 2.22 \times 10^{-10}\ T + 7.43 \times 10^{-8}$	14900
Copper	$3.55 \times 10^2 + 1.00 \times 10^{-1}\ T$	$4.21 \times 10^2 + 7.00 \times 10^{-2}\ T$	$(5.50 + 3.80 \times 10^{-2}\ T)\ \times 10^{-9}$	8960

$$\phi_c = h_c \cdot (T_i - T_w) \tag{4}$$

with ϕ_c the convective heat flux, T_w the water temperature, T_i the Inconel wall surface temperature, and h_c the convective coefficient (200 W m^{-2} K^{-1}).

The electric and thermal contacts at the inner interfaces obey Eqs. (5) and (6):

$$J_c = \sigma_c(U_1 - U_2) \tag{5}$$

$$\dot{q}_c = h_{cr}(T_1 - T_2) \tag{6}$$

with: J_c and $\dot{q}_c$ the current density and the heat flux across the contact, σ_c the electric contact conductance, h_{cr} the thermal contact conductance, and U_i and, T_i the electric potential and temperature on each side of the contact interface.

References

1. Orrù R, Licheri R, Locci AM, Cincotti A, Cao G (2009) Consolidation/synthesis of materials by electric current activated/assisted sintering. Mater Sci Eng R 63:127–287

2. Munir ZA, Quach DV, Ohyanagi M (2011) Electric current activation of sintering: a review of the pulsed electric current sintering process. J Am Ceram Soc 94:1–19

3. Vasiliev PO, Shen Z, Hodgkins RP, Bergström L (2006) Meso/macroporous, mechanically stable silica monoliths of complex shape by controlled fusion of mesoporous spherical particles. Chem Mater 18:4933–4938

4. Jiang D, Hulbert DM, Kuntz JD, Anselmi-Tamburini U, Mukherjee AK (2007) Spark plasma sintering: a high strain rate low temperature forming tool for ceramics. Mater Sci Eng A 463:89–93

5. Cai K, Romàn-Manso B, Smay JE, Zhou J, Osendi MI, Belmonte M, Miranzo P (2012) Geometrically complex silicon carbide structures fabricated by robocasting. J Am Ceram Soc 95:2660–2666

6. Monceau D, Oquab D, Estournes C, Boidot M, Selezneff S, Ratel-Ramond N (2010) Thermal barrier systems and multi-layered coatings fabricated by spark plasma sintering for the protection of Ni-base superalloys. Mater Sci Forum 654–656:1826–1831

7. Voisin T, Durand L, Karnatak N, Le Gallet S, Thomas M, Le Berre Y, Castagné JF, Couret A (2013) Temperature control during spark plasma sintering and application to up-scaling and complex shaping. J Mater Proc Technol 213:269–278

8. Olevsky E, Khaleghi E, Garcia C, Bradbury W (2010) Fundamentals of spark plasma sintering: applications to net-shaping of high strength temperature resistant components. Mater Sci Forum 654–656:412–415

9. Chanthapan S, Rape A, Gephart S, Kulkarni AK, Singh J (2011) Industrial scale field assisted sintering: an emerging disruptive manufacturing technology: applications. Adv Mater Proc 169: 25–28

10. McWilliams B, Yu J, Zavaliangos A (2015) Fully coupled thermal-electric-sintering simulation of electric field assisted sintering of net-shape compacts. J Mater Sci 50:519–530. doi:10.1007/s10853-014-8463-1

11. Pavia A, Durand L, Ajustron F, Bley V, Chevallier G, Peigney A, Estournès C (2013) Electro-thermal measurements and finite element method simulations of a spark plasma sintering device. J Mater Process Technol 213:1327–1336

12. Zavaliangos A, Zhang J, Krammer M, Groza JR (2004) Temperature evolution during field activated sintering. Mater Sci Eng A 379:218–228

13. Maizza G, Grasso S, Sakka Y, Noda T, Ohashi O (2007) Relation between microstructure, properties and spark plasma sintering (SPS) parameters of pure ultrafine WC powder. Sci Technol Adv Mater 8:644–654

14. Maizza G, Grasso S, Sakka Y (2009) Moving finite-element mesh model for aiding spark plasma sintering in current control mode of pure ultrafine WC powder. J Mater Sci 44:1219–1236. doi:10.1007/s10853-008-3179-8

15. Cincotti A, Locci AM, Orrù R, Cao G (2007) Modeling of SPS apparatus: temperature, current and strain distribution with no powders. AIChE J 53:703–719

16. Anselmi-Tamburini U, Gennari S, Garay JE, Munir ZA (2005) Fundamental investigations on the spark plasma sintering/synthesis process: II. Modeling of current and temperature distributions. Mater Sci Eng A 394:139–148

17. Vanmeensel K, Laptev A, Hennicke J, Vleugels J, Van der Biest O (2005) Modelling of the temperature distribution during field assisted sintering. Acta Mater 53:4379–4388

18. Ritasalo R, Cura ME, Liu XW, Söderberg O, Ritvonen T, Hannula SP (2010) Spark plasma sintering of submicron-sized Cu-powder—influence of processing parameters and powder oxidization on microstructure and mechanical properties. Mater Sci Eng A 527:2733–2737

19. Sule R, Olubambi PA, Sigalas I, Asante JKO, Garrett JC (2014) Effect of SPS consolidation parameters on submicron Cu and Cu-CNT composites for thermal management. Powder Technol 258:198–205

20. Robinson P (1990) Properties and selection nonferrous alloys and special-purpose materials, ASM handbook vol. 2. ASM International, Novelty, p 267

21. Brindley BJ, Worthington PJ (1970) Yield-point phenomena in substitutional alloys. Met Rev 15:101–114

22. Zhang ZH, Wang FC, Wang L, Li SK (2008) Ultrafine-grained copper prepared by spark plasma sintering process. Mater Sci Eng A 476:201–205

23. Grasso S, Sakka Y, Maizza G (2009) Pressure effects on temperature distribution during spark plasma sintering with graphite sample. Mater Trans 50:2111–2114

24. Li W, Olevsky EA, McKittrick J, Maximenko AL, German RM (2012) Densification mechanisms of spark plasma sintering: multi-step pressure dilatometry. J Mater Sci 47:7036–7046. doi:10.1007/s10853-012-6515-y